Is a more physical representation of aerosol activation needed for simulations of fog?

Craig Poku[1], Andrew N. Ross[1], Adrian A. Hill[2], Alan M. Blyth[1, 3], and Ben Shipway[2]

[1]School of Earth and Environment, University of Leeds
[2]Met Office, Exeter
[3]National Centre of Atmospheric Sciences, University of Leeds

Correspondence: Craig Poku (C.Y.A.Poku@leeds.ac.uk)

Abstract. Aerosols play a crucial role in the fog life cycle, as they determine the droplet number concentration, and hence droplet size, which in turn controls both the fog's optical thickness and life span. Detailed aerosol-microphysics schemes which accurately represent droplet formation and growth are unsuitable for weather forecasting and climate models, as the computational power required to calculate droplet formation would dominate the treatment of the rest of the physics in the

5 model. A simple method to account for droplet formation is the use of an aerosol activation scheme, which parameterises the droplet number concentration based on a change in supersaturation at a given time. Traditionally, aerosol activation parameterisation schemes were designed for convective clouds and assume that supersaturation is reached through adiabatic lifting, with many imposing a minimum vertical velocity (e.g. 0.1 m s^{-1}) to account for unresolved sub-grid ascent. In radiation fog, the measured updrafts during initial formation are often insignificant, with radiative cooling being the dominant process leading to

10 saturation. As a result, there is a risk that many aerosol activation schemes will overpredict the initial fog number concentration, which in turn may result in the fog transitioning to an optically thick layer too rapidly.

This paper presents a more physically-based aerosol activation scheme that can account for a change in saturation due to non-adiabatic processes. Using an offline model, our results show that the minimum updraft velocity threshold assumption can overpredict the droplet number by up to 70% in comparison to a cooling rate found in fog formation. The new scheme has

15 been implemented in the Met Office Natural Environment Research Council (NERC) Cloud (MONC) LES model, and tested using observations of a radiation fog case study based in Cardington, UK. The results in this work show that using a more physically-based method of aerosol activation leads to the calculation of a more appropriate cloud droplet number. As a result, there is a slower transition to an optically thick (well-mixed) fog that is more in-line with observations.

The results shown in this paper demonstrate the importance of aerosol activation representation in fog modelling, and the

20 impact that the cloud droplet number has on processes linked to the formation and development of radiation fog. Unlike the previous parameterisation for aerosol activation, the revised scheme is suitable to simulate aerosol activation in both fog and convective cloud regimes.

1 Introduction

Fog can be defined as a cloud at ground level with a surface visibility of less than 1 km (WMO, 1966). It can cause major disruption to road, aviation and marine transport, with associated economic losses that are comparable to those resulting from winter storms and hurricanes (Gultepe et al., 2007). Fog can have negative impacts on human health and the safety of certain activities. For example, thick fog on 5th September 2013 resulted in the Sheppey crossing crash in southeast England, consequently injuring 60 people (BBC, 2013). Understanding the physics behind fog is crucial in improving fog forecasting and mitigating the impact of such events.

A source of uncertainty in fog forecasting is the representation of aerosol-fog interactions. The Earth's atmosphere contains small suspended particles called aerosols, which range in size and composition (Pruppacher and Klett, 2010). Aerosols are important for both clouds and fog, as they act as the substrate on which water condenses and droplets form. The growth rate of these droplets is dependent on the initial aerosol size and solubility. The aerosols are considered to be 'activated' once these droplets reach a certain size, where they can grow more easily within a saturated environment (known as cloud condensation nuclei (CCN)). The aerosol population has been shown to impact the cloud's microphysical structure and its life span (e.g. Twomey, 1974; Albrecht, 1989), and these impacts have been studied in great depth over the last few decades, both in the context of climate (e.g. IPCC, 2001) and meteorology (e.g. Seifert and Heus, 2013; Miltenberger et al., 2018). While research into radiation fog spans the last 100 years (e.g. Taylor, 1917; Roach et al., 1976), studies investigating aerosol impacts on fog are more recent. For example, Bott (1991) shows that aerosols fundamentally control the optical thickness of radiation fog, and additional studies (e.g. Stolaki et al., 2015; Maalick et al., 2016) have verified the importance of capturing the aerosol indirect effects when simulating fog.

Accurate representation of droplet nucleation, i.e. aerosol activation, is essential to represent the indirect effects of aerosols on clouds. However, when investigating aerosol-cloud interactions in models such as general circulation models (GCMs) and numerical weather prediction (NWP) models, many detailed droplet growth schemes are unsuitable, as the computational power required would dominate the treatment of the rest of the physics in the model (Ghan et al., 1993). Original development of an aerosol activation parameterisation began by Squires (1958), with work by Twomey (1959) expanding on the modelling of aerosol activation. Twomey (1959) discussed the link between an aerosol spectrum, supersaturation and droplet number concentration. Using Köhler Theory, Twomey (1959) formulated a parameterisation based on the change in supersaturation for a given time, such that:

$$\frac{ds}{dt} = \alpha - \beta s \int_0^s \nu(\sigma) \left[\int_{\tau(\sigma)}^t s\, dt \right]^{\frac{1}{2}} d\sigma, \tag{1}$$

where α is the source of supersaturation due the cooling of a parcel and the second term of Eq. (1) representing the condensation of water vapour onto the activated aerosol. The constant, β, is dependent on the aerosol spectrum, with $\nu(\sigma)\delta\sigma$ being the number of nuclei in a unit volume with critical supersaturation between σ and $\sigma + \delta\sigma$. As condensation results in a decrease in

supersaturation, the maximum number of activated aerosols is capped and will occur once the peak supersaturation is reached

55 (i.e. when the condensation term starts to dominate the cooling terms), resulting in no more aerosols activating. At this point, $\frac{ds}{dt} = 0$, and Eq. (1) becomes:

$$\alpha = \beta s \int\limits_{0}^{s} \nu(\sigma) \left[\int\limits_{\tau(\sigma)}^{t} s\, dt \right]^{\frac{1}{2}} d\sigma. \tag{2}$$

Different authors have addressed solving the right hand side of Eq. (2). Twomey (1959) formulated an upper and lower bound to the inner integral in Eq. (2) and assumed an aerosol spectrum, which was later developed further by Cohard et al. (1998),

60 Shipway and Abel (2010) and Shipway (2015). Ghan et al. (1993) developed a scheme that accounted for a more realistic aerosol size distribution, which was naturally bounded by the total aerosol number. They showed that accounting for a more realistic single mode aerosol-size distribution (lognormal) improved the parameterised number of droplets activated. However, because droplet growth was neglected upon activation in their scheme, the introduction of multi-mode aerosol resulted in big discrepancies between the explicit and parameterised number of activated droplets. Work by Abdul-Razzak et al. (1998) (and

65 later Abdul-Razzak and Ghan, 2000) combined the benefits of the parameterisations developed by both Twomey (1959) and Ghan et al. (1993). The scheme was not only bound by the total aerosol number, but also assumed that growth continued from the point of activation. The result of these assumptions led to the parameterised number of activated aerosols agreeing better with the explicit calculation for activation, even in regimes of high updraft velocities (Abdul-Razzak and Ghan, 2000).

So far, the schemes discussed in this section (i.e. Cohard et al., 1998; Abdul-Razzak et al., 1998; Abdul-Razzak and Ghan,

70 2000; Shipway, 2015) have been tested assuming that saturation is driven by adiabatic ascent. In addition, a number of the listed schemes impose a fixed minimum updraft velocity threshold, w_{min}, of 0.1 m s^{-1}, corresponding to a cooling rate of 3.51 K hr^{-1} assuming a dry adiabatic lapse rate (e.g. Ghan et al., 1997; Abdul-Razzak and Ghan, 2000; Morrison and Gettelman, 2008; West et al., 2014). A w_{min} is suitable for these schemes, as they are designed to consider updrafts found in stratocumulus and convective clouds (Abdul-Razzak and Ghan, 2000; Meskhidze et al., 2005). Furthermore, some models (such as GCMs) will

75 use the subgrid velocity (derived from the subgrid turbulence) to calculate the number of droplets. However, the turbulence driven by cloud-top radiative cooling can be poorly resolved above the planetary boundary layer (PBL) unless the model's vertical resolution was < 100 m (Ghan et al., 1997). Since such resolutions are not feasible in operational NWP or climate models, a w_{min} of 0.1 m s^{-1} is imposed to account for this unresolved turbulence (Ghan et al., 1997). In radiation fog, the main mechanism for the initial formation of droplets is radiative cooling; a non-adiabatic process, with measured cooling rates

80 of 1 - 4 K hr^{-1} at the surface (calculated using data from Price, 2011) and updraft velocities close to 0 m s^{-1}. Consequently, both the assumption of saturation being driven by adiabatic ascent, and the use of a minimum vertical velocity threshold do not accurately account for aerosol activation in fog (as discussed in Boutle et al., 2018).

This paper will focus on addressing both of these assumptions in the modified Shipway (2015) aerosol activation scheme. It was chosen to use Shipway over Abdul-Razzak and Ghan (2000) (hereafter referred to as ARG), as it has been shown that ARG

85 overestimates condensation in low aerosol regimes, making it activate too few aerosols (Shipway, 2015). The work presented

in this paper has been split into two sections: firstly comparing the original Shipway scheme (henceforth Shipway) with the modified Shipway scheme developed here (SMOD) using an offline box model, and secondly comparing both of these schemes using large eddy simulation (LES) of an idealised fog case study (as described in Poku et al., 2019). During both comparisons, the following questions will be addressed:

90   1. What are the potential differences in aerosol activation between the Shipway and SMOD scheme?

2. How do the differences in aerosol activation representation impact on the fog evolution in a large eddy simulation?

Section 2 will present how the Shipway and SMOD scheme differ from each other mathematically. Section 3 will outline the Shipway box model setup and how the SMOD was implemented into it. Section 4 addresses research question 1. Section 5 describes the LES model used and addresses research question 2. A discussion and conclusion will then follow.

95   2   SMOD - Modifying the Shipway activation scheme to include non-adiabatic cooling

2.1   Shipway activation scheme

The Shipway (2015) aerosol activation scheme is designed as an improvement to the original lower bound approximation by Twomey (1959), and utilises a lookup table method that solves the maximum supersaturation at a reduced computational expense. Shipway assumes the differential activity spectrum, $\phi(s)$, to be lognormal, which can be expressed as:

$$100 \quad \phi(s) = \sum_{i=1}^{I} \frac{N_i}{\sqrt{2\pi}\ln(\sigma_{s,i})s} \exp\left(-\frac{\ln^2(s/s_{0,i})}{\ln^2\sigma_{s,i}}\right), \tag{3}$$

where N_i is the number concentration of dry aerosol, $\sigma_{s,i}$ is the standard deviation of the distribution of $\phi(s)$, and $s_{0,i}$ is the mean geometric supersaturation for each given aerosol mode. Shipway (2015) formulated a new expression for the maximum supersaturation using the original Twomey (1959) lower bound approximation, such that:

$$\frac{\sqrt{2}\alpha^{\frac{3}{2}}}{\gamma} = s_{max} \int_0^{s_{max}} \phi(\sigma) \left[\frac{1}{2}\left(1-\left(\frac{\sigma}{s_{max}}\right)^{\mu}\right)^{\lambda}\right]^{-1} \left(s_{max}^2 - \sigma^2\right)^{\frac{1}{2}} d\sigma, \tag{4}$$

105   where μ and λ are chosen empirically by Shipway (2015) such that $\mu = 3$ and $\lambda = 0.6$. α relates to the increase in relative humidity and hence saturation, due to an air parcel undergoing atmospheric cooling. To date, the Shipway activation scheme assumes that α is driven by an updraft velocity, i.e.

$$\alpha = \psi(T,p)\frac{dz}{dt}, \tag{5}$$

where $\psi(T)$ is the thermodynamical function associated with a change in supersaturation and pressure due to adiabatic
110   ascent, with:

$$\psi = \frac{c_p}{R_a T} - \frac{L}{R_v T^2}, \tag{6}$$

and γ being a temperature pressure variable related to the change in temperature due to latent heat release, such that:

$$\gamma = \frac{p}{\epsilon e_s} + \frac{L^2}{R_v c_p T^2}. \tag{7}$$

Using a precalculated lookup table to solve the right-hand side of Eq. (4) and again s_{max}, Shipway (2015) calculates the
115   total number of activated aerosols, N_{act}:

$$N_{act} = \frac{N_i}{2} \left[1 + \mathrm{erf} \left(\frac{\ln(s_{max}/s_{0,i})}{\sqrt{2} \ln \sigma_{s,i}} \right) \right], \tag{8}$$

with $\mathrm{erf}(x)$ being the error function (Abramowitz and Stegun, 1965). For the SMOD scheme (see Appendix A for further
details), the term, α, in Eq. (4) has been modified to account for non-adiabatic cooling, such that:

$$\alpha = \psi_1 \left. \frac{dT}{dt} \right|_{ad} + \psi_2 \left. \frac{dT}{dt} \right|_{non\_ad}, \tag{9}$$

120   where:

$$\psi_1 = \frac{c_p}{R_a T} - \frac{L}{R_v T^2},$$
$$\psi_2 = -\frac{L}{R_v T^2}. \tag{10}$$

The SMOD scheme differs from Shipway when calculating N_{act}, in that it uses Eq. (9) to solve s_{max} (see Table A1 in
Shipway, 2015, for a summary of terms described in this section and Appendix A for a full derivation of $\psi_{1,2}$).

3   The Shipway box model - offline setup

125   To understand the flexibility of the SMOD scheme and how the thermodynamical function associated with the non-adiabatic
contribution may impact N_{act}, both the Shipway and extended SMOD activation schemes will be directly compared using the
Shipway box model (Shipway, 2015). The Shipway box model is designed as a non-interactive offline suite to calculate the
initial number of activated aerosols in a range of different environmental settings. As the model is non-interactive, it permits

Table 1. Aerosol properties used to test the Shipway and SMOD schemes in the Shipway box model (Whitby, 1978).

Environmental setting	Distribution parameters	Aitken mode	Accumulation mode	Coarse mode
Marine	N (cm^{-3})	340	60	3.1
	σ	1.6	2.0	2.7
	r (μm)	0.005	0.035	0.31
Clean continental	N (cm^{-3})	1000	800	0.72
	σ	1.6	2.1	2.2
	r (μm)	0.008	0.034	0.46
Urban	N (cm^{-3})	10600	32000	5.4
	σ	1.8	2.16	2.21
	r (μm)	0.007	0.027	0.43

analysis of parameter space, in the absence of atmospheric feedbacks. Inputs of the model are potential temperature, vertical
130 velocity and aerosol population properties (number concentration, size, mode and distribution size parameters). Shipway (2015)
used the box model to test the Shipway (2015) and Twomey (1959) activation schemes in different aerosol regimes, in addition
to schemes developed by Abdul-Razzak and Ghan (2000) and Nenes and Seinfeld (2003).

For this work, the Shipway activation scheme was modified to account for a temperature change due to both adiabatic and
non-adiabatic processes, using Eq. (9). Aerosol loadings from Whitby (1978) were used to test both activation schemes. These
135 properties considered different environments, ranging from clean to polluted (Table 1). The temperature was set as a fixed
value of 274 K, based on surface temperatures observed during fog formation (Price, 2011; Haeffelin et al., 2013). All tests
were driven by cooling rates found in fog formation (1 - 4 K hr^{-1} calculated using data from Price, 2011), and also accounted
for a temperature change due to a nocturnal clear sky cooling (0 - 1 K hr^{-1}; Kiehl and Trenberth, 1997).

Table 2 displays the setup of four cases used in the offline box model, including the list of tests conducted in each case. Case
140 C_adiabatic directly compared Shipway and SMOD scheme, based on Eq.'s (4) and (9). To check that the SMOD scheme was
correctly coded into the box model, meaning that supersaturation can be driven by a cooling rate rather than an updraft velocity,
the non-adiabatic term in SMOD was set to zero. Conducting this case would also test the aerosol activation's sensitivity to the
choice in aerosol mode, as well as testing how both Shipway and SMOD would behave with no w_{min} being present.

Case C_accumulation_mar aimed to understand the maximum impact that different aerosol activation representations may
145 have on accumulation mode marine aerosols. For this case, three representations were used:

1. SMOD, which accounted for both adiabatic and non-adiabatic cooling. For these tests, $w_{min} = 0$ m s^{-1} and the adiabatic
   cooling component was switched off;

2. Default Shipway scheme. Cooling is assumed to be adiabatic, with $w_{min} = 0.1$ m s^{-1};

Table 2. The tests conducted in the offline box model.

Case	Tests in case	Scheme used	Cooling source	w_{min} applied	Aerosol mode	Environment
C_adiabatic	T_ship_ad	Shipway	Adiabatic		All modes	All environments
	T_SMOD_ad	SMOD	Adiabatic			
C_accumulation_mar	T_ship_mar_acc	Shipway	Adiabatic		Accumulation	Marine
	T_ship_mar_acc_wmin	Shipway	Adiabatic	x		
	T_SMOD_mar_acc	SMOD	Non-adiabatic			
C_accumulation_con	T_ship_con_acc	Shipway	Adiabatic		Accumulation	Clean continental
	T_ship_con_acc_wmin	Shipway	Adiabatic	x		
	T_SMOD_con_acc	SMOD	Non-adiabatic			
C_accumulation_urb	T_ship_urb_acc	Shipway	Adiabatic		Accumulation	Urban
	T_ship_urb_acc_wmin	Shipway	Adiabatic	x		
	T_SMOD_urb_acc	SMOD	Non-adiabatic			

3. Shipway scheme, with cooling assumed to be adiabatic and w_{min} = 0 m s^{-1} (i.e. assuming no additional sub-grid cooling). This might be more appropriate for use in an LES where vertical motion is well resolved.

Firstly, a comparison between Shipway with no w_{min} and Shipway in its default setting (with an applied w_{min} = 0.1 m s^{-1}) tested the suitability of a w_{min} in fog modelling. This comparison was motivated by Boutle et al. (2018), who discussed how aerosol activation in fog can be overestimated by the use of an applied w_{min}. The results of this test will quantify this overestimation, and hence provide potential a solution for fog modelling that may require some form of a w_{min}. Next, a comparison between SMOD and Shipway with w_{min} = 0 m s^{-1} tested the suitability of assuming adiabatic cooling in a non-adiabatic environment.

C_accumulation_mar was repeated for a clean continental and urban environment (test's C_accumulation_con and C_ accumulation_urb respectively) to understand how the aerosol activation representation impacts may change based on the environment choice.

4 Testing Shipway and SMOD using an offline box model

4.1 C_adiabatic - behaviours of the Shipway scheme in low updraft velocity regimes

The objective of C_adiabatic is to understand the relative importance of different aerosol modes concerning aerosol activation in fog and to check that the adiabatic pathway in the SMOD scheme was coded correctly. Although the implementation for
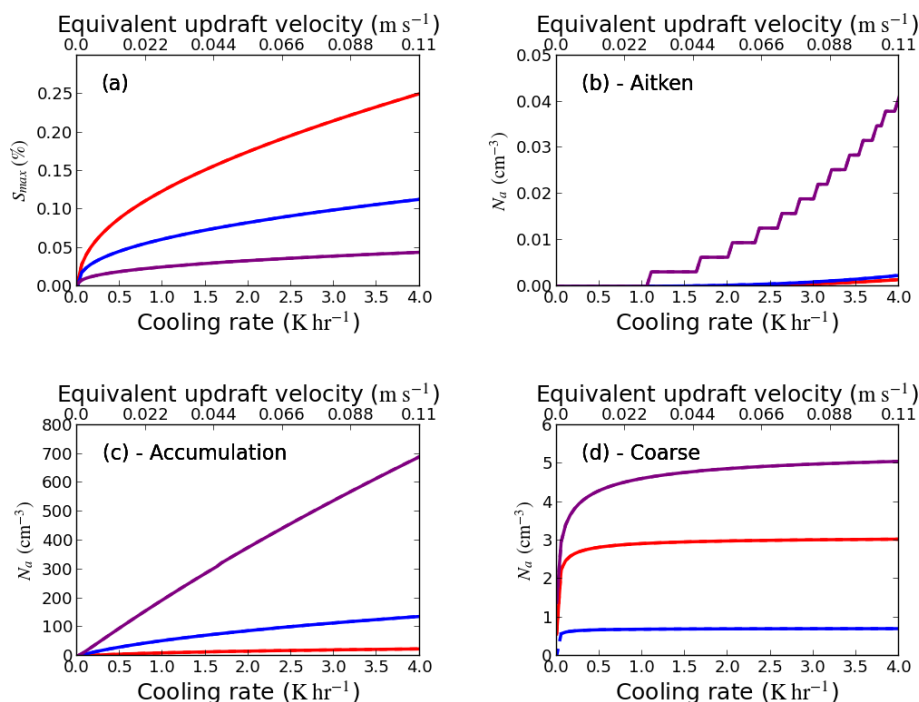
Figure 1. (a) Maximum supersaturation, s_{max} (%), against the total cooling rate. (b) - (d) A plot of activated aerosol concentration, N_{act} (cm^{-3}) against the total cooling rate for Aitken, accumulation and coarse mode aerosols respectively. Red - marine; Blue - clean continental; Purple - urban. Solid line - T_ship_ad; Dashed line - T_SMOD_ad (solid line overlaying the dashed line).

SMOD is different in that it applies a cooling rate rather than an updraft velocity, these tests comparing Shipway to SMOD should produce identical results for a given equivalent cooling rate.

When comparing the code that would control the adiabatic pathways in the Shipway and SMOD scheme, the differences in numerical calculations agree are negligible across all tests, which is shown by the overlapping dashed line over the solid line for all tests in Fig. 1. Figure 1a shows a monotonic increase in the maximum supersaturation, s_{max}, across all environments with respect to updraft velocity. For a fair comparison, an equivalent cooling rate was calculated for the SMOD scheme using the dry adiabatic lapse rate assumption (see Eq. A6 in Appendix A). The s_{max} is 0.26% for the marine environment; corresponding to a cooling rate of 4 K hr^{-1}, and decreases as the aerosol concentration increases (0.11 and 0.04% for the clean continental and urban environment respectively). The decrease in s_{max} with increases in aerosol concentration relates to an increased competition of water vapour and hence condensation rate, resulting in a reduced likelihood of newly activated droplets.

Figures 1b-d show an increase in activated aerosols in relation to cooling rate. Of the three modes, the proportion of activated aerosols is greatest in the accumulation mode in all tested environments. This is even though in some environments (e.g. marine), the proportion of aerosol in the Aitken mode is greater than the accumulation mode (see Table 1). The relatively small radii of Aitken mode aerosol compared to the rest of the aerosol spectrum makes the required maximum supersaturation for activation significantly higher, as displayed in Fig. 1b. The reality is that supersaturation levels in fog have been shown to only
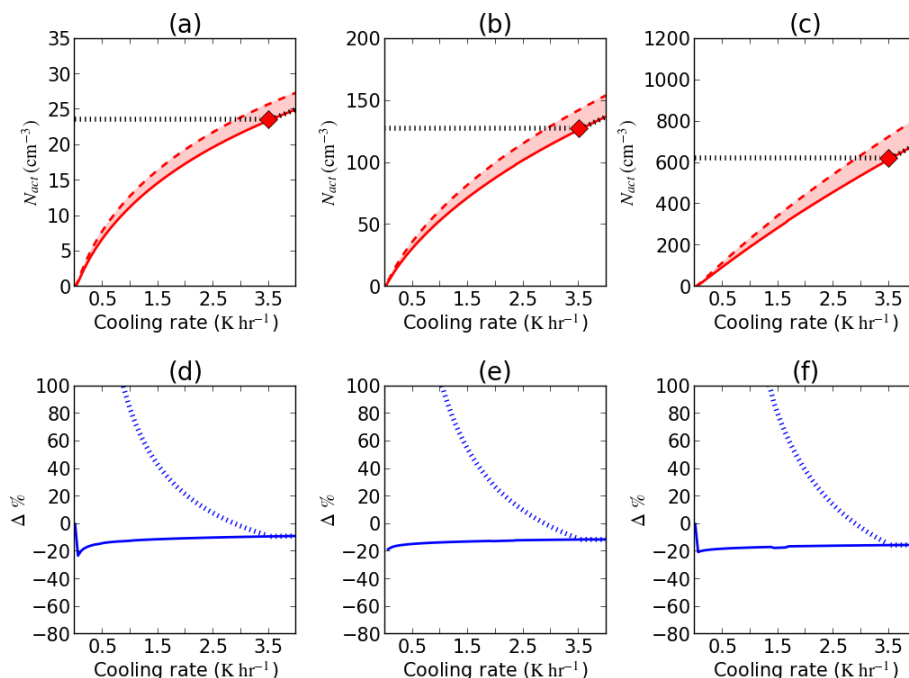
Figure 2. (a) Total activated aerosols, N_{act}, against the cooling rate for marine environment accumulation mode aerosols. Solid line - T_ship_mar_acc; dashed line - T_SMOD_mar_acc; black dashed line - T_ship_mar_acc_wmin. (d) Percentage differences, Δ %, between: dashed line - T_ship_mar_acc against T_ship_mar_acc_wmin; solid line - T_ship_mar_acc against T_SMOD_mar_acc. Red diamond - $w_{min} = 0.1$m s^{-1} (b), (e): clean continental; (c), (f): urban.

reach several tenths of 1% (Gerber, 1991), and hence would not be great enough to activate Aitken mode aerosol. Given the result of this test, it could indicate that nocturnal fog simulations that account for aerosol activation could neglect the Aitken mode. Although there is an increase in N_{act} with respect to updraft velocity for Aitken mode aerosol (Fig. 1b), the aerosol activation fraction is so small that it leads to a visible stepwise function (this being strongest in the urban environment). The stepwise behaviour for the Aitken mode is a result of poor resolution in the look-up table for the Shipway scheme at low updraft velocities, where this behaviour has been highlighted due to w_{min} not being present. The resolution could be improved by using a more robust integration method. However, changing the integration method does not impact the general conclusions relating to the new scheme and hence this will be explored in later work.

4.2 Associated percentage difference for methods of aerosol activation

To understand how N_{act} may be impacted by the choice in aerosol activation representation, accumulation mode tests in C_adiabatic were rerun using the SMOD activation scheme and the Shipway (2015) scheme with an applied w_{min}. Although these same tests were run for Aitken and coarse mode aerosol (see Table 1), there was little to no change in N_{act} when the aerosol activation representation was changed (not shown). In case C_accumulation_mar, T_SMOD_mar_acc produces a

higher N_{act} than T_ship_mar_acc for all cooling rates (Fig. 2a - marine), with a similar pattern being applicable to the clean
continental and urban environments (Figs. 2b and c). As the SMOD scheme for these tests assumes non-adiabatic cooling
exclusively, the increase in N_{act} is due to the associated thermodynamical function being independent of adiabatic lifting and
195   hence a change in pressure (see Appendix A for further details). Therefore, this demonstrates the dependency on the total
number of activated aerosols on the way in which the cooling is applied. To understand the impact of a w_{min} threshold on
N_{act}, all tests using the Shipway activation scheme were rerun, with the w_{min} threshold of 0.1 m s^{-1} being applied (Tests
T_ship_mar_acc_wmin, T_ship_con_acc_wmin and T_ship_urb_acc_wmin). Applying this threshold resulted in a fixed N_{act}
for a cooling rate below 3.51 K hr^{-1}. Consequently, should there be a cooling rate lower than this threshold, N_{act} will be
200   overestimated and this may impact properties of the fog evolution such as the fog's optical depth.

Figures 2d, e and f show the percentage difference between the SMOD and Shipway (with an applied w_{min}) activation
schemes increases as the prescribed cooling rate decreases. When comparing the three environments, the rate of increase in
the percentage difference grows, as the tested environment becomes more polluted. For example, a cooling rate of 1.5 K hr^{-1}
results in a percentage difference of 40, 50 and 70% for the three environments respectively. Given the associated percentage
205   difference, this indicates aerosol activation in fog simulations is overestimating N_{act} by an appreciable amount. However,
reducing the minimum threshold, w_{min}, to give an equivalent cooling rate close to those observed in fog would reduce but not
remove the problem associated with the percentage difference. Between the SMOD and Shipway schemes for aerosols in the
accumulation mode, the associated percentage change ranges between -10 and -20% for all three environments, and the rate
of change in the percentage difference is not appreciably different for any given environment (Figs. 2d, e and f). This implies
210   that even if the minimum threshold of w_{min} were to be reduced such that it is representative for updraft velocities found in
radiation fog, just using the Shipway scheme could potentially underestimate aerosol activation.

5   Testing Shipway and SMOD using MONC

The offline box model results demonstrate that assumptions widely used in aerosol activation (e.g. Abdul-Razzak and Ghan,
2000) may be significantly overestimating aerosol activation in fog. In this section, the impact of this overestimation on fog
215   development in large-eddy simulations of fog is assessed using MONC. These tests have two objectives. The first objective is
assessing the impact the assumption $w_{min} = 0.1$ m s^{-1} has on the simulated fog. The second objective is to understand how
the SMOD scheme for aerosol activation impacts on the fog evolution and the causes of differences from the Shipway scheme.

5.1   MONC model - online setup

As part of this work, MONC is used to perform a suite of sensitivity tests based on intensive observation period 1 (IOP1) from
220   the recent Local And Non-local Fog EXperiment (LANFEX) field campaign (Price et al., 2018). A full description of IOP1
and the observed vertical profiles the model was initialised with, can be found in Poku et al. (2019). The model setup for IOP1
is presented in Table 3. A domain size of 132×132 m^2 was chosen, as there is minimal impact on the fog's turbulent kinetic
energy (TKE) and liquid water when compared to simulations that were tested on a larger domain (not shown). The choice

Table 3. The input parameters and model setup for IOP1 in MONC.

IOP1 input parameters	Values
Horizontal domain	132 x 132 m
Vertical domain	705 m
Δx, Δy	2 m
Δz	Variable - 1 m first 100 m, streched up to 6 m afterwards
Simulation duration	12 hr
Timestep	0.1 s
Surface geostrophic winds	u_g = 1.3 m s^{-1}, v_g = 2.1 m s^{-1}
Cloud microphysics	Cloud AeroSol Interactive Microphysics (CASIM)
Radiative transfer scheme	Suite of Community RAdiative Transfer codes (SOCRATES) (Edwards and Slingo, 1996)

of grid spacing was motivated by studies such as Maalick et al. (2016) and Maronga and Bosveld (2017), which both show
225 the fog formation's sensitivity to the model resolution. Therefore, it was critical to run MONC at such a high resolution. The
model's surface boundary conditions were prescribed with a varying surface temperature (described in Poku et al., 2019) and a
surface vapour mixing ratio of 0.004 kg kg^{-1}, which were both based on observations. Radiation was calculated using the Suite
of Community RAdiative Transfer codes (SOCRATES), based on the work of Edwards and Slingo (1996). SOCRATES was
called by the MONC model every 5 min, allowing for the longwave radiative fluxes at the top of the fog layer to be captured in
230 the model.

All simulations use the Cloud AeroSol Interactive Microphysics (CASIM) scheme; a multi-moment bulk microphysics
scheme designed to simulate aerosol-cloud interactions (Grosvenor et al., 2017; Dearden et al., 2018; Miltenberger et al.,
2018). For this work, CASIM has been set to 2 moments and is being used to represent a non-precipitating, warm boundary
layer cloud (i.e. ice processes and autoconversion to rain are turned off). In CASIM, the cloud-drop size distribution, $N(D)$,
235 assumes a gamma distribution, which has the form (Shipway and Hill, 2012):

$$N(D) = N_0 D^{\mu_d} e^{-\lambda_d D}, \tag{11}$$

where N_0 is the distribution intercept parameter, μ_d is the shape parameter (the default value of μ_d is set to 0), λ_d is the
slope parameter and D is the droplet diameter. For this work, μ_d has been set to equal 3.0, based on observations of the liquid
water path (LWP) and cloud-drop size distribution during IOP1, resulting in a more sensible modelled sedimentation rate (see
240 Appendix B for details). With regards to aerosol sizes, only accumulation mode aerosol where 0.1 μm < CCN size diameter <
1 μm) are accounted for, as at the time of development, MONC was unable to run with a multi-mode aerosol setting. Aerosol
activation is being represented using both the original Shipway scheme and the new modified SMOD scheme.

Table 4. Details of the simulations using the Shipway and SMOD activation scheme. The value of w_{min} has been lowered from 0.1 to 0.01 m s^{-1} based on the results from Sec. 4. Cooling rate equivalent calculated using the dry adiabatic lapse rate assumption.

Test no.	Test name	Scheme	Imposed w_{min} (m s^{-1})	Threshold cooling rate equivalent (K hr^{-1})	r_e (μm)
T1	T_shipway_wmin	Shipway	0.1	3.51	10
T2	T_shipway_0.01	Shipway	0.01	0.351	10
T3	T_SMOD	SMOD	N/A	N/A	10
T4	T_er_15	SMOD	N/A	N/A	15
T5	T_er_20	SMOD	N/A	N/A	20

During IOP1, there were no direct aerosol or CCN measurements. Therefore, a CCN value of 100 cm^{-3} in the accumulation mode was set, with a total soluble mass of 2.7ng throughout the initialised vertical profile and an assumed lognormal size

245 distribution with a standard deviation of 2.0, based on typical measurements for a clean rural site similar to Cardington, UK (Boutle et al., 2018; Poku et al., 2019). To reduce computational expense and data storage, 1D diagnostics are output every 1min and 3D diagnostics are output every 5min.

SMOD was implemented into MONC based on Eq. (9), which involves adding the adiabatic and non-adiabatic contributions together for the combined cooling rate to them be used for aerosol activation. The adiabatic contribution for this equation

250 was derived from the resolved positive updraft velocity in MONC. The non-adiabatic contribution to date only consists of the longwave heating tendency that is derived using SOCRATES. For reference, the implementation of these partitioned terms is done similarly to the aerosol activation scheme used by Vie et al. (2016). Although it has been acknowledged that there are other non-adiabatic contributions to changes in supersaturation such as turbulent mixing, further model development would be required to account for these changes. However, given that radiative cooling is the biggest source of saturation during fog

255 formation (Roach et al., 1976), these results should provide useful insight into the representation of aerosol activation during a stable fog case.

Table 4 displays all tests that will evaluate Shipway against SMOD. The first objective will be addressed by comparing test's T1 - T3, and outcome of this comparison will result in a clear understanding of how different activation representations could influence the cloud droplet number concentration (CDNC) evolution in IOP1. To date, the effective radius, r_e, has the option to

260 be fixed or for it to vary with a change in CDNC. In order to isolate the impact of aerosol activation on number concentration, this work used a fixed r_e. As the non-adiabatic contribution in the SMOD scheme is directly influenced by r_e, two tests were setup testing its sensitivity, and hence will motivate future work that involves deciding whether a coupled effective radius is required when using the SMOD scheme.
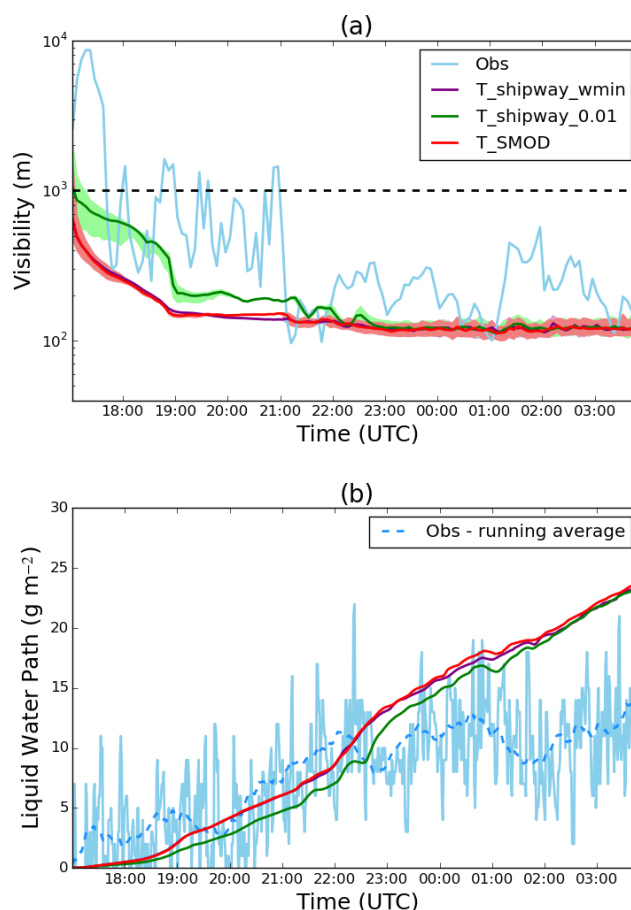
Figure 3. (a) - Time series of the near-surface mean visibility (Vis; m) at a 2 m altitude. Purple – T_shipway_wmin; green – T_shipway_0.01; red – T_SMOD; light blue – observations. Minimum and maximum visibility are marked on the figure by the shaded area. (b) - Time series of the liquid water path (g m^{-2}). Purple – T_shipway_wmin; green – T_shipway_0.01; red – T_SMOD; light blue – observations; blue dashed - running average over observations (40 points).

5.2 Comparing simulations using the Shipway and SMOD scheme

265   Fog forms in tests T_shipway_wmin, T_shipway_0.01 and T_SMOD at 1700 UTC, and all decrease to a mean near-surface visibility of 120 m by the end of the night (Fig. 3a). For all model simulations, visibility, Vis, is calculated using the formula of Gultepe et al. (2006):

$$Vis = \frac{1.002}{(LWC \times CDNC)^{0.6473}}, \tag{12}$$

where LWC is the liquid water content and $CDNC$ is the cloud droplet number concentration. Equation (12) was derived

270 based on observations of fog in mainland Europe and is valid over a range of CDNC from a few per cubic centimetre up to a few hundred per cubic centimetre (Gultepe et al., 2006).

Despite the differences in near-surface visibility, all three tests have the strongest rate of decrease between 1700 and 1845 UTC (Fig. 3a). During this time, the mean near-surface visibility in T_shipway_wmin, T_shipway_0.01 and T_SMOD decrease to 208, 151 and 210 m respectively. However, T_shipway_0.01 has a noticeably higher near-surface visibility before 1830 UTC

275 and best agrees with observations, before decreasing in visibility at the same rate as T_shipway_wmin. Upon first inspection, it appears that just lowering w_{min} is the solution to prevent the simulation overestimating aerosol activation in fog, as shown by T_shipway_0.01. However, the model's spin-up period lasted around an hour in these simulations, meaning that the CDNC calculation is likely being influenced by initial prescribed random perturbations, as opposed to turbulence driven by either wind shear or convective motion. Unfortunately, with the earliest radiosonde data available being at 1700 UTC, the features

280 in T_shipway_0.01 could not be avoided (for context, the observations show a stable boundary layer (SBL) beginning to form around the time of model initialisation). Nonetheless, the lower threshold used in T_shipway_0.01 allows for the simulation to undergo a slower transition in near-surface visibility to a thicker fog. This suggests that the number of activated droplets calculated may account for inaccurate representation of what was observed during IOP1.

Throughout the night, both T_shipway_wmin and T_SMOD have a higher LWP than T_shipway_0.01 (Fig. 3b). Poku et al.

285 (2019) showed that the LWP increases with aerosol concentration and hence CDNC, with Porson et al. (2011) demonstrating that the increase in CDNC resulted in a stronger downwelling longwave flux, signalling the presence of a deeper fog. T_shipway_wmin has the steepest decrease in the visibility during fog formation, suggesting that it has the highest initial CDNC. As these tests all have the same fixed effective radius (unlike studies such as Stolaki et al., 2015), the change in LWP is primarily due to the sedimentation rate, therefore indicating that T_shipway_wmin has the slowest sedimentation rate of

290 all three tests as a result. A decreased sedimentation rate will lead to more liquid water being present in the fog layer. Consequently, this will lead to stronger cooling at the fog top (Poku et al., 2019), strengthening the feedback of increased liquid water production in the layer. This result provides further evidence of how the error in aerosol activation that utilises a w_{min} of $0.1\ \mathrm{m\ s^{-1}}$ impacts the fog, especially during the initial formation stage. The LWP and mean near-surface visibility are not appreciably different between T_shipway_wmin and T_SMOD (Fig. 3b), suggesting the CDNC is very similar between the

295 two. T_shipway_0.01 has the highest near-surface visibility between 1700 and 2300 UTC by up to 340 m, in addition to the lowest LWP by up to $4\ \mathrm{g\ m^{-2}}$. Averaged time-height slices of CDNC and LWC were taken for all three tests, showing relatively small changes in the fog layer's CDNC between T_shipway_wmin and T_SMOD (not shown).

The similarity of T_shipway_wmin and T_SMOD suggests that the combined cooling rate in T_SMOD is similar to the cooling rate associated with w_{min} in T_shipway_wmin. To understand whether this is the case, a horizontal slice at $z = 2$ m

300 of CDNC and the contributions to the relative cooling rates were taken at different times, as shown in Fig. 4. As 2 m is not at the model's lowest vertical grid box, there should not be any direct heating from the imposed surface conditions. At 1730 UTC the CDNC is about 83 $\mathrm{cm^{-3}}$ (Fig. 4a), with more than 85% of the total cooling contribution being due to longwave heating (Fig. 4m). However, later in the night, the cooling contribution to longwave tendencies increases to around 90% within
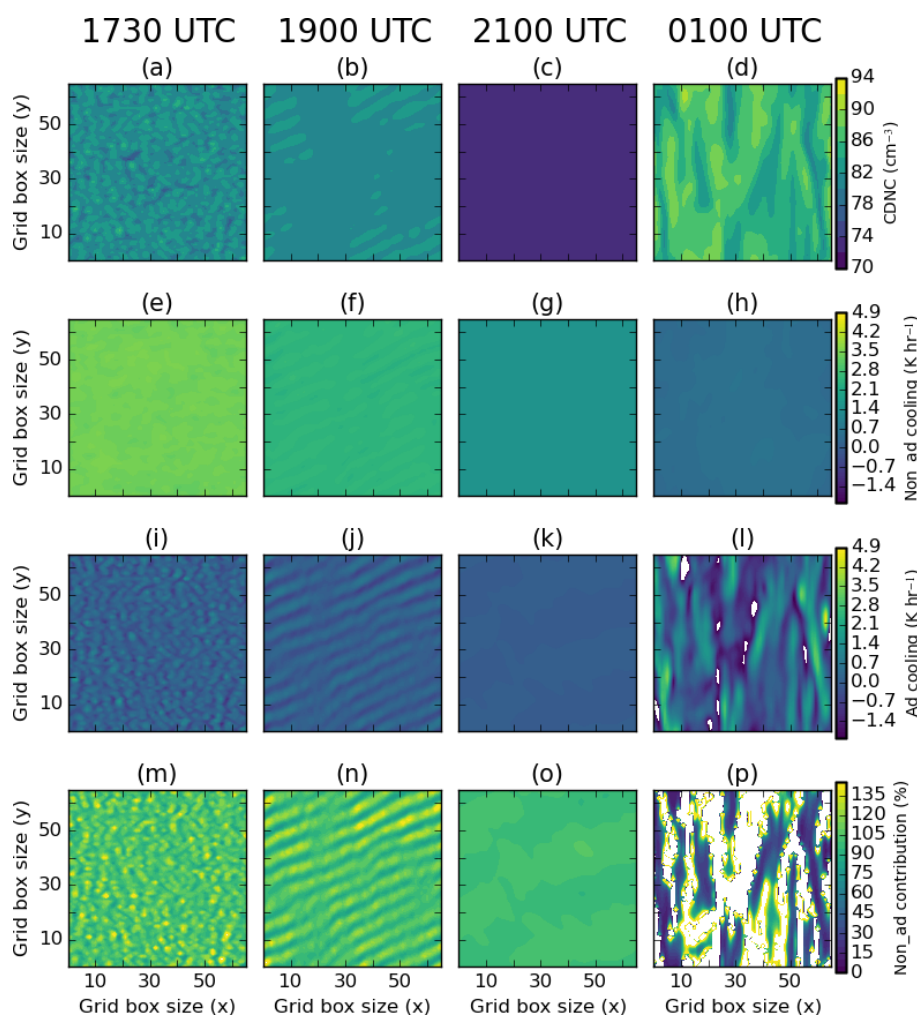
Figure 4. Horizontal slices made at z = 2 m of CDNC (cm^{-3}) in T_SMOD at (a) - 1730, (b) - 1900, (c) - 2100 and (d) - 0100 UTC. (e) - (h): non-adiabatic cooling (K hr^{-1}); (i) - (l): adiabatic cooling (K hr^{-1}); (m) - (p): Non-adiabatic cooling contribution (%). Note: for the cooling contribution, white masks out regions where the contribution is greater than 140 (%).

the fog layer (Fig. 4o), due to a decrease in the adiabatic cooling tendency to about 0.5 K hr^{-1} (Fig. 4k). Eventually, the fog

305 develops, resulting in the longwave contribution to cooling decreasing to around 15% (Fig. 4p), with an increase in cooling due to vertical motion. The drop in near-surface longwave cooling occurs as the fog transitions to become optically thick, and so the longwave flux divergence becomes smaller near the surface, while the adiabatic effects become larger due to the onset of convection driven by radiative cooling at the fog top (Mazoyer et al., 2017).

The new SMOD activation scheme is more physically realistic, in that it is coupled to the radiative cooling in the fog, making

310 the scheme potentially more sensitive to the way that this cooling is calculated in the model. Therefore, the assumption of the
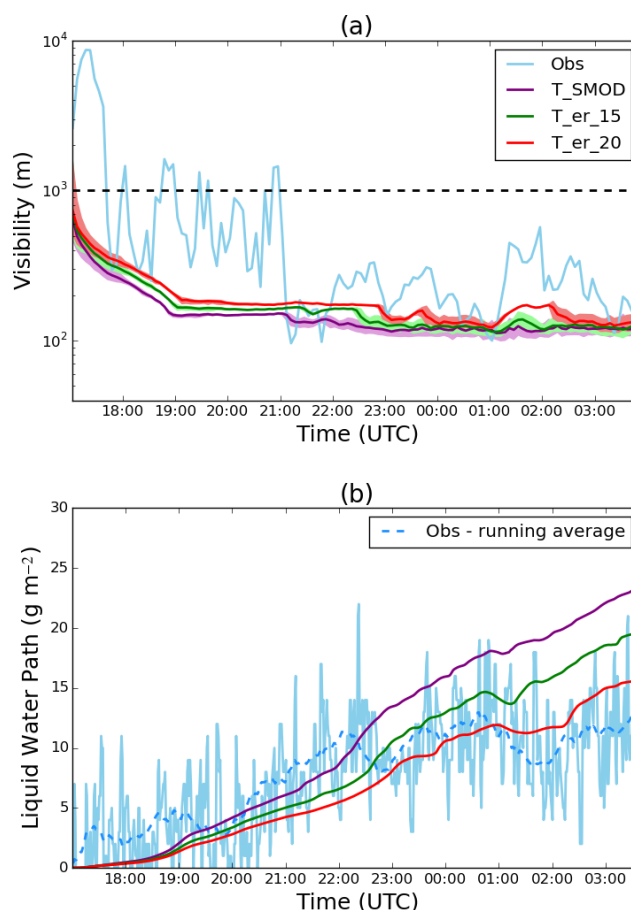
Figure 5. (a) - Time series of the mean visibility (m) at a 2 m altitude. Purple – T_SMOD; green – T_er_15; red – T_er_20; light blue – observations. The minimum and maximum visibility are marked on the figure by the shaded area. (b) - Time series of the liquid water path (g m^{-2}). Purple – T_SMOD; green – T_er_15; red – T_er_20; light blue – observations; blue dashed - running average over observations (40 points).

effective radius being fixed for these simulations may not be suitable to accurately simulate the radiative impact of the fog layer. The following section will present some sensitivity tests to assess the impact of this assumption on fog development.

5.2.1 Sensitivity of SMOD to the effective radius

Hill et al. (2008) showed the impact of using a fixed effective radius in simulations of stratocumulus clouds, with studies
315 such as Bierwirth et al. (2013) and Young et al. (2016) showing how the observed effective radius in arctic clouds can change (between 5 to 15 μm) in relation to the cloud's LWC and CDNC. As this variability may be key to modelling radiation fog using the SMOD activation scheme, two tests were conducted that investigated the fog's sensitivity to a change in r_e. When increasing r_e from 10 to 20 μm, the near-surface visibility increases by up to 40%, and decreases the LWP by up to 42% (Fig.

5). However, whilst increasing r_e results in the LWP agreeing better with observations, neither test captures the changes in near-
320 surface visibility during fog formation. Bergot et al. (2015) showed that the fog's spatial variability during initial formation had
been impacted when their simulations included a heterogeneous terrain. However, Cardington is relatively homogeneous and
hence potentially highlights a further discrepancy in the aerosol representation in these simulations. As an example, in-cloud
removal (nucleation scavenging) has not been accounted in this work, which has been shown to impact the spatial variability
and development of mixed-phased clouds (Miltenberger et al., 2018). Nonetheless, the decrease in liquid water indicates that
325 the fog's development in optical thickness has slowed down with an increase in r_e and hence the importance of coupling both
CASIM and SOCRATES together. Going forward, future studies should use a coupled r_e as this should, in theory, lead to
an improvement in CDNC as the better representation in aerosol activation in the SMOD scheme will feed into the radiation
scheme.

Figure 6 shows time-height slices of CDNC and LWC for T_SMOD, T_er_15 and T_er_20. Before 2145 UTC, the CDNC
330 in T_SMOD is strongest towards the top at around 80 cm^{-3}. After this time, it increases throughout the fog layer to a range
between 86 and 94 cm^{-3} (Fig. 6a). Coinciding with this is an increase in LWC from 0.2 to 0.24 g kg^{-1}, suggesting the time
at which the fog began to develop and grow in optical thickness. However, an increase in r_e results in delayed onset of the
growth in optical thickness to 2300 and 0030 UTC for T_er_15 and T_er_20 respectively. The CDNC on average decreases
for both T_er_15 and T_er_20 across the whole fog layer, with a noticeable rise at around 2300 UTC for T_er_15. Although
335 this pattern is the same for T_er_20, there are periods where there are visible decreases in CDNC, e.g. between 0130 and 0230
UTC (Figs. 6c and e respectively). A combination of both the CDNC and LWC decreasing results in a slower transition in the
fog layer, which is shown in the downwelling longwave at 2 m (Fig.7). The downwelling longwave decreases by a maximum
of 20 W m^{-2} between T_SMOD and T_er_20, with T_er_20 undergoing the slowest rate of increase. There are differences
between the observed and simulated downwelling in all three simulations, however, before 2200 UTC, T_er_20 decreases this
340 difference to a maximum of 10 W m^{-2}.

SOCRATES calculates the longwave radiative fluxes by the cloud's optical depth, τ, (Edwards and Slingo, 1996):

$$\tau = k^{(e)}\Delta m, \tag{13}$$

such that Δm is the change in mass for a given spectral band and $k^{(e)}$ is the mass extinction coefficient, which is defined as:

$$k^{(e)} = L\left(a + \frac{b}{r_e}\right). \tag{14}$$

345 For SMOD scheme, both the CDNC and LWC is sensitive to r_e, given Eq's (13) and (14). This leads to a more physical
representation of aerosol activation that should be considered when simulating cases of fog. These results demonstrate the
importance of an accurate effective radius and the reasons for using a coupled r_e, given its impact on the fog evolution.
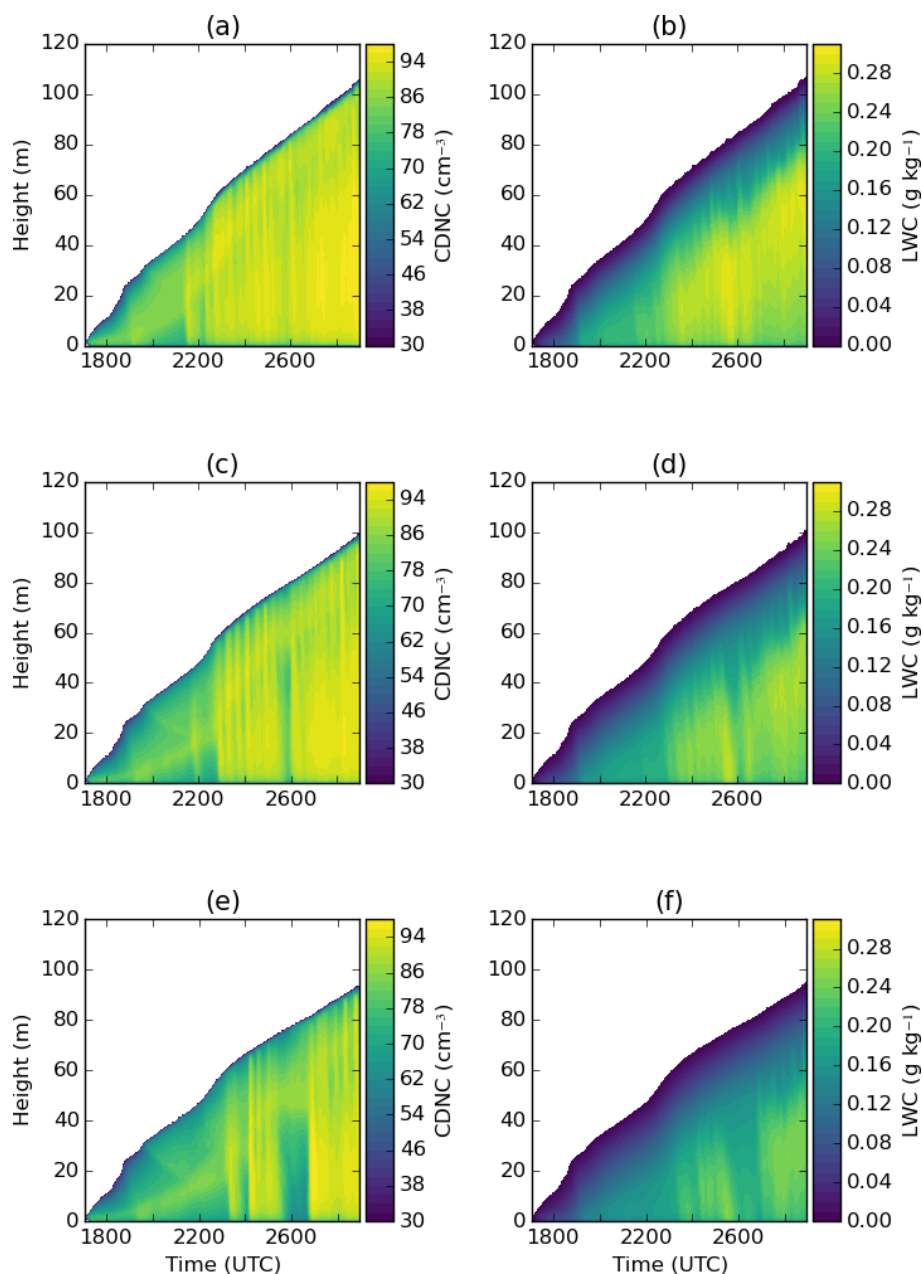
Figure 6. Plots of (a), (c), (e) - mean CDNC (cm^{-3}); and (b), (d), (f) - mean LWC (g kg^{-1}). (a), (b): T_SMOD; (c), (d): T_er_15; (e), (f); T_er_20.
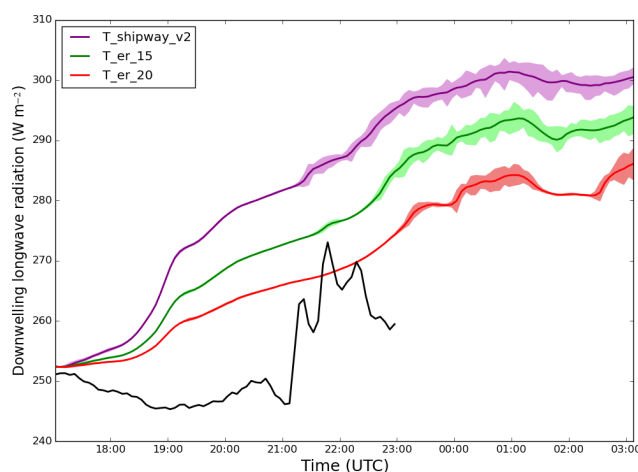
Figure 7. Time series of the downwelling longwave radiation (W m^{-2}) at a 2 m altitude. Purple – T_SMOD; green – T_er_15; red – T_er_20; black – observations. The minimum and maximum downwelling longwave radiation are marked on the figure by the shaded area.

6 Discussion

This work aimed to investigate how the representation of aerosol activation influenced simulations of nocturnal radiation fog.
350 There was a strong focus on critiquing the assumptions used in several current aerosol activation schemes, which are usually designed for clouds where cooling is driven by adiabatic ascent. This work addressed two research questions.

6.1 What are the potential differences in aerosol activation between the Shipway and SMOD scheme?

The assumptions used in the Shipway (2015) scheme to date, i.e. the use of just an updraft velocity with a minimum threshold w_{min}, were tested against the SMOD scheme in an offline box model. The sensitivity of Shipway to w_{min} was first tested. For
355 accumulation and coarse mode aerosol, there was a monotonical decrease in N_{act} as w_{min} approached 0 m s^{-1}. These tests also highlighted the stepwise function present in Aitken mode aerosol in the low updraft velocity regime. Given the fraction of Aitken aerosols activated, our results may suggest that Aitken mode aerosol can be ignored when modelling activation in fog based on the range of environmental aerosol size distributions, as the required environmental supersaturation for impact is substantially higher than supersaturation's seen in reality. However, the stepwise behaviour was caused by the poor resolution
360 in the look-up table that calculated s_{max} in this regime, therefore demonstrating why just removing w_{min} with no alternative cooling source may not be an appropriate solution when simulating aerosol activation in fog.

For accumulation mode aerosol, there were noticeable percentage differences between the actual cooling rate and the use of a w_{min} equal to 0.1 m s^{-1} (as typically used in clouds) by up to 70%, as the environment becomes more polluted. In reality, for a given liquid water path, increasing the aerosol concentration will result in a larger concentration of smaller droplets, increasing
365 the fog's optical depth (Twomey, 1977), and may cause the fog to become well-mixed too quickly. Therefore for this example, a similar effect could occur should an unsuitable w_{min} be used in fog simulations. In addition, these tests demonstrated that using

an aerosol activation scheme that assumes just adiabatic ascent may potentially underestimate N_{act} by 20% in an environment driven by non-adiabatic cooling processes (i.e. fog formation). Furthermore, the associated percentage difference in the choice of w_{min} would be the same should SMOD be run with just an adiabatic cooling source, given there were no differences in

370 C_adiabatic. Consequently, both of these results show that the aerosol indirect effects may not be properly accounted for in simulations of fog when using a traditional aerosol activation scheme.

6.2 How do the differences in aerosol activation representation impact on the fog evolution in a large eddy simulation?

The Shipway (2015) aerosol activation scheme was used to test the impact w_{min} could have on simulating fog in MONC using

375 only accumulation mode aerosol. It was shown that a reduction in w_{min} lowered the initial CDNC during formation, resulting in the fog undergoing a slower transition to a well-mixed layer. Reducing w_{min} to 0.01 m s^{-1} displayed some unusual model behaviours during fog formation, which is most likely driven by the model's spin-up period, rather than shear or convection motion. However, the only way to confirm this is to initialise the model earlier, which is not possible with the given radiosonde data from IOP1. Upon initial analysis, there was not an improved performance using the SMOD scheme against the Shipway

380 scheme with an applied w_{min} of 0.1 m s^{-1}. However, it was shown that the cause of this result was due to r_e not reflecting the change in CDNC. When r_e was increased from 10 to 20 μm, the result was a slower transition to a well-mixed layer, which was more in line with observations of IOP1. This highlighted the importance of the effective radius and provides further motivation to couple the effective radius with a change in CDNC.

7 Conclusions

385 This work has demonstrated the unsuitability of using an aerosol activation scheme designed for convective clouds in fog simulations. This complements previous studies such as Schwenkel and Maronga (2019), who have shown how the choice in aerosol activation scheme impacts the fog evolution through a change in the CDNC. However, by designing a scheme that is also dependent on a non-adiabatic cooling source, the results in this paper have demonstrated the importance of aerosol activation representation when trying to accurately capture the fog's transition to a well-mixed layer. Previous studies (e.g.

390 Mazoyer et al., 2017) have investigated the fog evolution while accounting for a radiative cooling tendency in the change in supersaturation. However, this is the first study that has investigated the change in cooling due to non-adiabatic processes in a clean aerosol regime, making it beneficial in aiding the understanding the impact of aerosol-fog interactions during nocturnal radiation fog.

Work to develop the SMOD scheme is still ongoing and will include accounting for additional non-adiabatic processes such

395 as turbulent or subgrid mixing. Completing this work could make it easier to incorporate the SMOD scheme into a model such as an NWP model. This is because the non-adiabatic process would be a change in temperature within the grid box, rather than requiring an explicit additional term. It was shown that SMOD is sensitive to SOCRATES with regards to the fixed effective radius, especially when considering the decrease in CDNC. Therefore, future work should run the new scheme with the

interactive coupling of r_e to CASIM, should the option be available. As noted in Section 5.2, SMOD was unable to capture the
400 fog's spatial variability during initial formation. However, Miltenberger et al. (2018) showed that by including in-cloud aerosol
removal, the source of aerosol began depleting through nucleation, resulting in a more open-cell cloud structure and changes
in the cloud dynamics. To date, there are no studies that have investigated the use of a nucleation scavenging parameterisation
in fog in the context of bulk microphysical parameterisations, therefore suggesting a future piece of work within the subject of
aerosol-fog interactions. For this work, there was a lack of simultaneous measurements of observed aerosol and cloud droplets.
405 Given the w_{min}'s sensitivity to aerosol concentration, having these measurements in future studies will both help constrain the
model and highlight any further discrepancies in aerosol activation representation in fog.

As a wider implication, aerosol-cloud interactions are a big source of uncertainty when modelling atmospheric processes,
both within forecasting (NWP) and climate (GCM) models and the choice of aerosol activation can influence how big this
uncertainty is. Typically, the resolution of NWP and GCM model simulations is very coarse compared to LES, meaning that any
410 present updraft velocities are usually subgrid and hence cannot be resolved. To represent aerosol activation on a subgrid level,
the vertical velocity is either in the form a characteristic vertical velocity (e.g. Ghan et al., 1997) or a PDF function based on
the vertical velocity (e.g. West et al., 2014). More recently, Malavelle et al. (2014), for example, discussed methods to account
for subgrid velocities used in aerosol activation in convection-permitting models. These methods utilise a w_{min}, however,
this should be lowered systematically for future work regarding aerosol activation in fog. Although gaining measurements of
415 vertical velocity PDFs could be difficult in fog, the results presented in this paper could provide a useful framework to estimate
what the variation in vertical velocities in fog could be, therefore providing a good estimation of the types of distributions that
best match these velocities. Finally, to have a full cooling term applied in an NWP model, it is important to know how these
vertical velocities correlate with the changes in non-adiabatic cooling.

This paper has shown the need to differentiate between optically thin fog ($w_{min} \approx 0 \text{ m s}^{-1}$) and optically thick fog, where
420 sub-grid vertical velocities can be important. The method being presented in this work is computationally efficient and provided
an additional level of flexibility consider different cooling sources in cases where updrafts are not the dominant cooling source.
Given this flexibility, this will allow the SMOD scheme to undergo further testing in both high resolution and NWP models.
Whilst this has been tested in only the Shipway and SMOD activation schemes, the framework for a change in supersaturation
is generic enough for it to be applied to other activation schemes too.

425 **Appendix A: Mathematical formulation for the change in supersaturation**

Pruppacher and Klett (2010) defined supersaturation in terms of the water vapour mixing ratio, q_v, as:

$$q_v = (1+s)\left(\frac{\epsilon e_s}{p}\right),\tag{A1}$$

where p is the pressure of dry air, s is the environment's supersaturation, e_s is the saturation vapour pressure and $\epsilon = \dfrac{R_a}{R_v} = 0.622$; the ratio of the gas constant of dry air to water vapour. Differentiating Eq. (A1) with respect to time, and rearranging for the change in supersaturation gives:

$$\frac{ds}{dt} = \left(\frac{p}{\epsilon e_s}\right)\frac{dq_v}{dt} - (1+s)\left[\frac{1}{e_s}\frac{de_s}{dt} - \frac{1}{p}\frac{dp}{dt}\right]. \tag{A2}$$

The Clausius-Clapeyron equation is defined as:

$$\frac{de_s}{dT} = \frac{Le_s}{R_v T^2}. \tag{A3}$$

Applying the chain rule gives:

$$\frac{de_s}{dt} = \frac{Le_s}{R_v T^2}\left.\frac{dT}{dt}\right|_{tot}. \tag{A4}$$

$$= \frac{Le_s}{R_v T^2}\left[\left.\frac{dT}{dt}\right|_{ad} + \left.\frac{dT}{dt}\right|_{non\_ad} + \left.\frac{dT}{dt}\right|_{lat}\right].$$

$\left.\dfrac{dT}{dt}\right|_{ad}$ is the change in temperature due to dry adiabatic processes, such that:

$$\left.\frac{dT}{dt}\right|_{ad} \equiv -\Gamma\frac{dz}{dt} = -\Gamma\,w; \tag{A5}$$

where $\Gamma = \dfrac{g}{c_p}$, the dry adiabatic lapse rate and w is the updraft velocity. $\left.\dfrac{dT}{dt}\right|_{non\_ad}$ is the change in temperature due to non-adiabatic processes (e.g. radiative cooling, turbulent mixing), that excludes latent heat release, and $\left.\dfrac{dT}{dt}\right|_{lat}$ is the change in temperature due to latent heat release i.e. condensation/evaporation. For adiabatic expansion (lifting), there are corresponding pressure and temperature changes (that satisfy the first law of thermodynamics). However, for isobaric non-adiabatic heating processes, there is no change in p but there is a change in T that modifies Eq. (A4). Therefore, for the change in p, by:

1. assuming hydrostatic equilibrium, where $\dfrac{dp}{dz} = -\rho g$;

2. using the equation for the ideal gas law, where $p = \rho R_a T$;

$$\frac{dp}{dt} = \frac{dp}{dz}\frac{dz}{dt}$$

$$= -\frac{pg}{R_a T}w. \tag{A6}$$

The change in temperature due to latent heat release is proportional to the change in vapour mixing ratio, such that:

$$\frac{dT}{dt}\bigg|_{lat} = -\frac{L}{c_p}\frac{dq_v}{dt}\bigg|_{cond} = \frac{L}{c_p}\frac{dq_l}{dt}. \tag{A7}$$

Inserting Eq.'s (A4), (A6) and (A7) into Eq. (A2), and assuming $1 + s \approx 1$ gives:

$$\frac{ds}{dt} = \left(\frac{Lg}{R_v T^2 c_p} - \frac{g}{R_a T}\right)w - \frac{L}{R_v T^2}\frac{dT}{dt}\bigg|_{non\_ad} - \left(\frac{p}{\epsilon e_s} + \frac{L^2}{R_v c_p T^2}\right)\frac{dq_l}{dt}. \tag{A8}$$

450   Eq. (A8) can be used to simulate aerosol activation in both fog and convective cloud regimes, highlighting the flexibility of the SMOD scheme. As an objective for this work is to understand how using an adiabatic framework to represent aerosol activation in an non-adiabatic environment (e.g. fog) may impact N_{act}, w in Eq.(A8) will be rewritten as $\frac{dT}{dt}\big|_{ad}$, such that:

$$\frac{ds}{dt} = \psi_1 \frac{dT}{dt}\bigg|_{ad} + \psi_2 \frac{dT}{dt}\bigg|_{non\_ad} - \gamma\frac{dq_l}{dt}, \tag{A9}$$

where:

$$\psi_1 = \frac{c_p}{R_a T} - \frac{L}{R_v T^2},$$

455   $$\psi_2 = -\frac{L}{R_v T^2}, \tag{A10}$$

$$\gamma = \frac{p}{\epsilon e_s} + \frac{L^2}{R_v c_p T^2}.$$

Appendix B: Fitting modelled LWP and cloud drop-size distribution to observations - shape parameter

All tests in this paper assume a fixed r_e, implying that the change in liquid water is controlled by the sedimentation rate, as discussed in Poku et al. (2019). The sedimentation rate is controlled by the cloud drop-size distribution (see Eq. 11), with its skewness being determined by the shape parameter, μ_d. Mazoyer et al. (2017) adapted the default shape parameter to best fit

460   the modelled cloud drop-size distribution to observations. For this work, a similar approach would have ideally been chosen to find a suitable μ_d to capture the changes in liquid water. However, the instrumentation only began to record spectra during IOP1 4 hours into the observed fog case, and by this time, the layer had already begun to grow in optical thickness. To account for this limitation, the LWP was used to decide on a suitable choice of μ_d. These simulations were then compared to the available IOP1 cloud spectra data, to validate and hence choose a μ_d going forward. For this fitting, μ_d ranged from 0 to 3, with these

465   tests denoted as T_mu_0, T_mu_1, T_mu_2 and T_mu_3 respectively. Although simulations were conducted to increase the shape parameter up to a value of $\mu_d = 7$ (similar to Mazoyer et al., 2017), the LWP for tests where $\mu_d > 4$ were higher than the observed mean LWP and hence these results will not be shown.
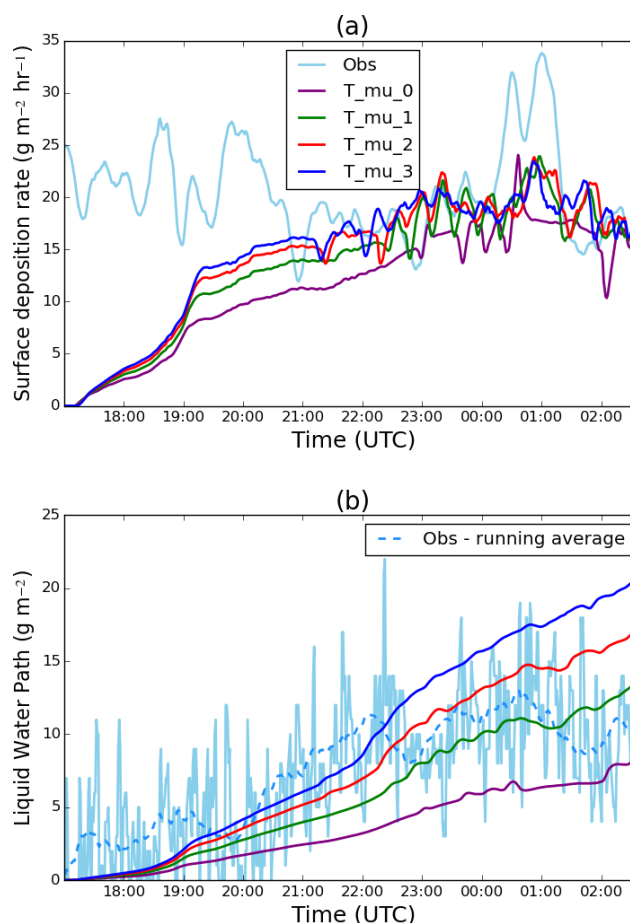
Figure B1. a) - Time series of the surface deposition rate (g m^{-2} hr^{-1}). Purple – T_mu_0; green – T_mu_0; red – T_mu_1; dark blue – T_mu_3; light blue – observations. (b) Time series of the liquid water path (g m^{-2}). Purple – T_control; green – T_mu_1; red – T_mu_2; dark blue – T_mu_3; light blue – observations; blue dashed – running average over observations (40 points).

Both the surface deposition rate and LWP increase with μ_d (Figs. B1a-b), with this increase being more inline with observations. T_mu_2 and T_mu_3 both show improved LWP when compared to observations, especially before 2200 UTC. As there are potentially multiple options in choosing μ_d, the modelled cloud drop-size distribution was compared to observations, as shown in Fig. B2. Prior to 2200 UTC, all shape parameter tests began with an abundance of small droplets, signalling the formation of fog, and the density of small droplets being greatest in T_mu_0 (not shown). During fog evolution, all tests begin moving right in terms of skewness with the exception for T_mu_0 (due to T_mu_0 being logarithmic). For the tests where $\mu_d > 0$, increasing the shape parameter results in the peak of the distribution decreasing and moving to the right, for all tested time frames. For example, increasing the shape parameter to $\mu_d = 3$ results in a peak droplet diameter of 11 μm. These results suggest a limitation in the default choice in $\mu_d = 0$ and hence the assumption of a logarithmic distribution for fog development
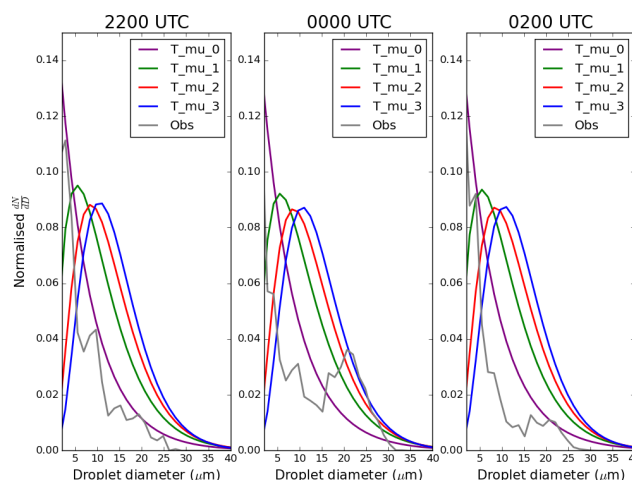
Figure B2. Cloud drop-size distributions for shape parameter simulations at 1710, 1800 and 2200 UTC at 2 m. T_mu_0; green – T_mu_0; red – T_mu_1; dark blue – T_mu_3; grey - observations.

during IOP1. By increasing the shape parameter during the fog evolution, fewer large droplets will sediment out of the fog layer, therefore explaining the presence of bigger droplets still within the system in these tests (for example, tests T_mu_1 - 3).

At 2200 UTC, the observed cloud droplet spectrum mostly follows a logarithmic distribution, however, later in the night, it evolves more into a bi-modal distribution (as seen in Price, 2011). For example, at 0000 UTC, the peaks occur at 8 and 22 μm. Of the shape parameter tests, the observations are in best agreement with T_mu_3 for droplet size diameters between 22 to 27 μm at 0000 UTC, however, this fit does not take into account the peak shown within the smaller droplets. In an ideal situation, a modelled cloud drop-size distribution would take into account the bi-modal nature shown within the distribution. In reality, it is likely that these smaller droplets have not activated, but instead are a source of hydrated aerosol which can contribute up to 68% of the total light scattered, and hence result in the reduction in visibility within the fog (Hammer et al., 2014). However, although these smaller droplets may potentially change the microphysical structure of the fog, the introduction of a bi-modal distribution (or a varying shape parameter) within CASIM may increase model computational expense, with no appreciable changes in the fog evolution. Given these results, a shape parameter of $\mu_d = 3$ will be used in this paper.

Author contributions. CP undertook the research, carried out the simulations and analysis, and led the writing of the paper. AR, AB, AH contributed to the research design, interpretation of the results and the writing of the final paper. AH provided technical support with MONC. BS provided the box model and supported its use.

Code availability. The MONC, CASIM, offline box model and SOCRATES codes are maintained by the Met Office and accessible via the Met Office Science Repository Service (https://code.metoffice.gov.uk/) (last access: 28th August 2020). The MONC branch is available

at https://code.metoffice.gov.uk/svn/monc/main/branches/dev/craigpoku/r6496_MONC_poku_activation (last access: 28th August 2020).
495 The CASIM branch is available at https://code.metoffice.gov.uk/svn/monc/casim/branches/dev/craigpoku/vn0.3.2_poku_scheme_debugged (last access: 28th August 2020). The offline box model branch is available at https://code.metoffice.gov.uk/svn/monc/casim/branches/dev/craigpoku/r287_Offline_Activation (last access: 28th August 2020). For further details, please contact Craig Poku (c.y.a.poku@leeds.ac.uk) or Adrian Hill (adrian.hill@metoffice.gov.uk)

Competing interests. The authors declare that there are no competing interests.

500 *Acknowledgements.* The authors would like to thank the Met Office Research Unit in Cardington (UK) for providing and processing the observational dataset used throughout this study. CP was supported by a Natural Environment Research Council (NERC) Industrial CASE award with the Met Office (grant number NE/M009955/1). This work used Monsoon2, a collaborative High Performance Computing facility funded by the Met Office and the Natural Environment Research Council.

References

505 Abdul-Razzak, H. and Ghan, S. J.: A parameterization of aerosol activation: 2. Multiple aerosol types, Journal of Geophysical Research: Atmospheres, 105, 6837–6844, https://doi.org/10.1029/1999JD901161, http://doi.wiley.com/10.1029/97JD03735, 2000.

Abdul-Razzak, H., Ghan, S. J., and Rivera-Carpio, C.: A parameterization of aerosol activation: 1. Single aerosol type, Journal of Geophysical Research: Atmospheres, 103, 6123–6131, https://doi.org/10.1029/97JD03735, 1998.

Abramowitz, M. and Stegun, I.: Handbook of mathematical functions, Courier Corporation, http://people.math.sfu.ca/~cbm/aands/intro.htm,
510 1965.

Albrecht, B. A.: Aerosols, cloud microphysics, and fractional cloudiness., Science, 245, 1227–30, https://doi.org/10.1126/science.245.4923.1227, http://www.ncbi.nlm.nih.gov/pubmed/17747885, 1989.

BBC: Sheppey crossing crash: Dozens hurt as 130 vehicles crash - BBC News, https://www.bbc.co.uk/news/uk-england-kent-23970047, 2013.

515 Bergot, T., Escobar, J., and Masson, V.: Effect of small-scale surface heterogeneities and buildings on radiation fog: Large-eddy simulation study at Paris-Charles de Gaulle airport, Quarterly Journal of the Royal Meteorological Society, 141, 285–298, https://doi.org/10.1002/qj.2358, http://doi.wiley.com/10.1002/qj.2358, 2015.

Bierwirth, E., Ehrlich, A., Wendisch, M., Gayet, J.-F., Gourbeyre, C., Dupuy, R., Herber, A., Neuber, R., and Lampert, A.: Climate of the Past Geoscientific Instrumentation Methods and Data Systems Optical thickness and effective radius of Arctic boundary-layer clouds
520 retrieved from airborne nadir and imaging spectrometry, Atmos. Meas. Tech, 6, 1189–1200, https://doi.org/10.5194/amt-6-1189-2013, www.atmos-meas-tech.net/6/1189/2013/, 2013.

Bott, A.: On the influence of the physico-chemical properties of aerosols on the life cycle of radiation fogs, Boundary-Layer Meteorology, 56, 1–31, https://doi.org/10.1007/BF00119960, http://link.springer.com/10.1007/BF00119960, 1991.

Boutle, I., Price, J., Kokkola, H., Romakkaniemi, S., Kudzotsa, I., Kokkola, H., and Romakkaniemi, S.: Aerosol-fog interaction and the
525 transition to well-mixed radiation fog, Atmos. Chem. Phys, 18, 7827–7840, https://doi.org/10.5194/acp-18-7827-2018, https://www.atmos-chem-phys-discuss.net/acp-2017-765/acp-2017-765.pdfhttps://doi.org/10.5194/acp-18-7827-2018, 2018.

Cohard, J.-M., Pinty, J.-P., and Bedos, C.: Extending Twomey's Analytical Estimate of Nucleated Cloud Droplet Concentrations from CCN Spectra, Journal of the Atmospheric Sciences, 55, 3348–3357, https://doi.org/10.1175/1520-0469(1998)055<3348:ETSAEO>2.0.CO;2, http://journals.ametsoc.org/doi/abs/10.1175/1520-0469%281998%29055%3C3348%3AETSAEO%3E2.0.CO%3B2, 1998.

530 Dearden, C., Hill, A., Coe, H., and Choularton, T.: The role of droplet sedimentation in the evolution of low-level clouds over southern West Africa, Atmos. Chem. Phys, 18, 14 253–14 269, https://doi.org/10.5194/acp-18-14253-2018, https://doi.org/10.5194/acp-18-14253-2018, 2018.

Edwards, J. M. and Slingo, A.: Studies with a flexible new radiation code. I: Choosing a configuration for a large-scale model, Quarterly Journal of the Royal Meteorological Society, 122, 689–719, https://doi.org/10.1002/qj.49712253107, http://doi.wiley.com/10.1002/qj.
535 49712253107, 1996.

Gerber, H.: Supersaturation and Droplet Spectral Evolution in Fog, Journal of the Atmospheric Sciences, 48, 2569–2588, https://doi.org/10.1175/1520-0469(1991)048<2569:SADSEI>2.0.CO;2, http://journals.ametsoc.org/doi/abs/10.1175/1520-0469%281991%29048%3C2569%3ASADSEI%3E2.0.CO%3B2, 1991.

Ghan, S. J., Chung, C. C., and Penner, J. E.: A parameterization of cloud droplet nucleation part I: single aerosol type, Atmospheric Research, 30, 198–221, https://doi.org/10.1016/0169-8095(93)90024-I, https://www.sciencedirect.com/science/article/pii/016980959390024I, 1993.

Ghan, S. J., Leung, L. R., Easter, R. C., and Abdul-Razzak, H.: Prediction of cloud droplet number in a general circulation model, Journal of Geophysical Research: Atmospheres, 102, 21 777–21 794, https://doi.org/10.1029/97JD01810, http://doi.wiley.com/10.1029/97JD01810, 1997.

Grosvenor, D. P., Field, P. R., Hill, A. A., and Shipway, B. J.: The relative importance of macrophysical and cloud albedo changes for aerosol-induced radiative effects in closed-cell stratocumulus: insight from the modelling of a case study, Atmospheric Chemistry and Physics, 17, 5155–5183, https://doi.org/10.5194/acp-17-5155-2017, https://www.atmos-chem-phys.net/17/5155/2017/, 2017.

Gultepe, I., Müller, M. D., Boybeyi, Z., Gultepe, I., Müller, M. D., and Boybeyi, Z.: A New Visibility Parameterization for Warm-Fog Applications in Numerical Weather Prediction Models, Journal of Applied Meteorology and Climatology, 45, 1469–1480, https://doi.org/10.1175/JAM2423.1, http://journals.ametsoc.org/doi/abs/10.1175/JAM2423.1, 2006.

Gultepe, I., Tardif, R., Michaelides, S. C., Cermak, J., Bott, A., Bendix, J., Müller, M. D., Pagowski, M., Hansen, B., Ellrod, G., and Others: Fog research: A review of past achievements and future perspectives, Pure and Applied Geophysics, 164, 1121–1159, 2007.

Haeffelin, M., Dupont, J. C., Boyouk, N., Baumgardner, D., Gomes, L., Roberts, G., and Elias, T.: A Comparative Study of Radiation Fog and Quasi-Fog Formation Processes During the ParisFog Field Experiment 2007, Pure and Applied Geophysics, 170, 2283–2303, https://doi.org/10.1007/s00024-013-0672-z, 2013.

Hammer, E., Gysel, M., Roberts, G. C., Elias, T., Hofer, J., Hoyle, C. R., Bukowiecki, N., Dupont, J.-C., Burnet, F., Baltensperger, U., and Weingartner, E.: Size-dependent particle activation properties in fog during the ParisFog 2012/13 field campaign, Atmos. Chem. Phys, 14, 10 517–10 533, https://doi.org/10.5194/acp-14-10517-2014, www.atmos-chem-phys.net/14/10517/2014/, 2014.

Hill, A. A., Dobbie, S., and Yin, Y.: The impact of aerosols on non-precipitating marine stratocumulus. I: Model description and prediction of the indirect effect, Quarterly Journal of the Royal Meteorological Society, 134, 1143–1154, https://doi.org/10.1002/qj.278, http://doi.wiley.com/10.1002/qj.278, 2008.

IPCC: Climate Change 2001: The Scientific Basis, Cambridge University Press, 2001.

Kiehl, J. T. and Trenberth, K. E.: Earth's Annual Global Mean Energy Budget, Bulletin of the American Meteorological Society, 78, 197–208, http://journals.ametsoc.org/doi/abs/10.1175/1520-0477%281997%29078%3C0197%3AEAGMEB%3E2.0.CO%3B2, 1997.

Maalick, Z., Kühn, T., Korhonen, H., Kokkola, H., Laaksonen, A., and Romakkaniemi, S.: Effect of aerosol concentration and absorbing aerosol on the radiation fog life cycle, Atmospheric Environment, 133, 26–33, 2016.

Malavelle, F. F., Haywood, J. M., Field, P. R., Hill, A. A., Abel, S. J., Lock, A. P., Shipway, B. J., and McBeath, K.: A method to represent subgrid-scale updraft velocity in kilometer-scale models: Implication for aerosol activation, Journal of Geophysical Research: Atmospheres, 119, 4149–4173, https://doi.org/10.1002/2013JD021218, http://doi.wiley.com/10.1002/2013JD021218, 2014.

Maronga, B. and Bosveld, F. C.: Key parameters for the life cycle of nocturnal radiation fog: a comprehensive large-eddy simulation study, Quarterly Journal of the Royal Meteorological Society, pp. 2463–2480, https://doi.org/10.1002/qj.3100, http://doi.wiley.com/10.1002/qj.3100, 2017.

Mazoyer, M., Lac, C., Thouron, O., Bergot, T., Masson, V., and Musson-Genon, L.: Large eddy simulation of radiation fog: impact of dynamics on the fog life cycle, Atmospheric Chemistry and Physics, 17, 13 017–13 035, https://doi.org/10.5194/acp-17-13017-2017, https://www.atmos-chem-phys.net/17/13017/2017/, 2017.

Meskhidze, N., Nenes, A., Conant, W. C., and Seinfeld, J. H.: Evaluation of a new cloud droplet activation parameterization with in situ data from CRYSTAL-FACE and CSTRIPE, Journal of Geophysical Research: Atmospheres, 110, 2005.

Miltenberger, A. K., Field, P. R., Hill, A. A., Rosenberg, P., Shipway, B. J., Wilkinson, J. M., Scovell, R., and Blyth, A. M.: Aerosol–cloud interactions in mixed-phase convective clouds – Part 1: Aerosol perturbations, Atmospheric Chemistry and Physics, 18, 3119–3145,
580   https://doi.org/10.5194/acp-18-3119-2018, https://www.atmos-chem-phys.net/18/3119/2018/, 2018.

Morrison, H. and Gettelman, A.: A New Two-Moment Bulk Stratiform Cloud Microphysics Scheme in the Community Atmosphere Model, Version 3 (CAM3). Part I: Description and Numerical Tests, Journal of Climate, 21, 3642–3659, https://doi.org/10.1175/2008JCLI2105.1, https://journals.ametsoc.org/doi/pdf/10.1175/2008JCLI2105.1, 2008.

Nenes, A. and Seinfeld, J. H.: Parameterization of cloud droplet formation in global climate models, Journal of Geophysical Research, 108,
585   https://doi.org/10.1029/2002JD002911, http://doi.wiley.com/10.1029/2002JD002911, 2003.

Poku, C., Ross, A. N., Blyth, A. M., Hill, A. A., and Price, J. D.: How important are aerosol–fog interactions for the successful modelling of nocturnal radiation fog?, Weather, pp. 237–243, https://doi.org/10.1002/wea.3503, https://rmets.onlinelibrary.wiley.com/doi/10.1002/wea.3503https://rmets.onlinelibrary.wiley.com/doi/10.1002/wea.3503, 2019.

Porson, A., Price, J., Lock, A., and Clark, P.: Radiation Fog. Part II: Large-Eddy Simulations in Very Stable Conditions, Boundary-Layer
590   Meteorology, 139, 193–224, https://doi.org/10.1007/s10546-010-9579-8, http://link.springer.com/10.1007/s10546-010-9579-8, 2011.

Price, J.: Radiation Fog. Part I: Observations of Stability and Drop Size Distributions, Boundary-Layer Meteorology, 139, 167–191, https://doi.org/10.1007/s10546-010-9580-2, 2011.

Price, J. D., Lane, S., Boutle, I. A., Smith, D. K. E., Bergot, T., Lac, C., Duconge, L., McGregor, J., Kerr-Munslow, A., Pickering, M., and Clark, R.: LANFEX: a field and modeling study to improve our understanding and forecasting of radiation fog, Bulletin of the
595   American Meteorological Society, pp. 2061–2077, https://doi.org/10.1175/BAMS-D-16-0299.1, http://journals.ametsoc.org/doi/10.1175/BAMS-D-16-0299.1, 2018.

Pruppacher, H. and Klett, J.: Microphysics of Clouds and Precipitation, vol. 18 of *Atmospheric and Oceanographic Sciences Library*, Springer, https://doi.org/10.1007/978-0-306-48100-0, http://link.springer.com/10.1007/978-0-306-48100-0, 2010.

Roach, W. T., Brown, R., Caughey, S. J., Garland, J. A., and Readings, C. J.: The physics of radiation fog: I - A field study, Quarterly Journal
600   of the Royal Meteorological Society, 102, 313–333, 1976.

Schwenkel, J. and Maronga, B.: Large-eddy simulation of radiation fog with comprehensive two-moment bulk microphysics: impact of different aerosol activation and condensation parameterizations, Atmospheric Chemistry and Physics, 19, 7165–7181, https://doi.org/10.5194/acp-19-7165-2019, https://www.atmos-chem-phys.net/19/7165/2019/, 2019.

Seifert, A. and Heus, T.: Large-eddy simulation of organized precipitating trade wind cumulus clouds, Atmospheric Chemistry and Physics,
605   13, 5631–5645, https://doi.org/10.5194/acp-13-5631-2013, https://www.atmos-chem-phys.net/13/5631/2013/, 2013.

Shipway, B. and Abel, S.: Analytical estimation of cloud droplet nucleation based on an underlying aerosol population, Atmospheric Research, 96, 344–355, https://doi.org/10.1016/J.ATMOSRES.2009.10.005, https://www.sciencedirect.com/science/article/pii/S0169809509002798?via%3Dihub, 2010.

Shipway, B. J.: Revisiting Twomey's approximation for peak supersaturation, Atmospheric Chemistry and Physics, 15, 3803–3814, 2015.

610 Shipway, B. J. and Hill, A. A.: Diagnosis of systematic differences between multiple parametrizations of warm rain microphysics using a kinematic framework, Quarterly Journal of the Royal Meteorological Society, 138, 2196–2211, https://doi.org/10.1002/qj.1913, http://doi.wiley.com/10.1002/qj.1913, 2012.

Squires, P.: The Microstructure and Colloidal Stability of Warm Clouds: Part II-The Causes of the Variations in Microstructure, Tellus, 10, 262–271, https://doi.org/10.3402/tellusa.v10i2.9228, https://www.tandfonline.com/doi/full/10.3402/tellusa.v10i2.9228, 1958.

615 Stolaki, S., Haeffelin, M., Lac, C., Dupont, J.-C., Elias, T., and Masson, V.: Influence of aerosols on the life cycle of a radiation fog event. A numerical and observational study, Atmospheric Research, 151, 146–161, 2015.

Taylor, G. I.: The formation of fog and mist, Quarterly Journal of the Royal Meteorological Society, 43, 241–268, https://doi.org/10.1002/qj.49704318302, http://doi.wiley.com/10.1002/qj.49704318302, 1917.

Twomey, S.: The nuclei of natural cloud formation part II: The supersaturation in natural clouds and the variation of cloud droplet concen-
620 tration, Pure and Applied Geophysics, 43, 243–249, 1959.

Twomey, S.: Pollution and the planetary albedo, Atmospheric Environment (1967), 8, 1251–1256, 1974.

Twomey, S.: The Influence of Pollution on the Shortwave Albedo of Clouds, Journal of the Atmospheric Sciences, 34, 1149–1152, 1977.

Vie, B., Pinty, J. P., Berthet, S., and Leriche, M.: LIMA (v1.0): A quasi two-moment microphysical scheme driven by a multimodal population of cloud condensation and ice freezing nuclei, Geoscientific Model Development, 9, 567–586, https://doi.org/10.5194/gmd-9-567-2016,
625 2016.

West, R. E. L., Stier, P., Jones, A., Johnson, C. E., Mann, G. W., Bellouin, N., Partridge, D. G., and Kipling, Z.: The importance of vertical velocity variability for estimates of the indirect aerosol effects, Atmos. Chem. Phys, 14, 6369–6393, https://doi.org/10.5194/acp-14-6369-2014, www.atmos-chem-phys.net/14/6369/2014/, 2014.

Whitby, K. T.: The physical characteristics of sulfur aerosols, Atmospheric Environment (1967), 12, 135–159, 1978.

630 WMO: International Meteorological Vocabulary, 1966.

Young, G., Jones, H. M., Choularton, T. W., Crosier, J., Bower, K. N., Gallagher, M. W., Davies, R. S., Renfrew, I. A., Elvidge, A. D., Darbyshire, E., Marenco, F., Brown, P. R. A., Ricketts, H. M. A., Connolly, P. J., Lloyd, G., Williams, P. I., Allan, J. D., Taylor, J. W., Liu, D., and Flynn, M. J.: Observed microphysical changes in Arctic mixed-phase clouds when transitioning from sea ice to open ocean, Atmos. Chem. Phys, 16, 13 945–13 967, https://doi.org/10.5194/acp-16-13945-2016, www.atmos-chem-phys.net/16/13945/2016/, 2016.